1   **Interfacing or Doping? Role of Ce in Highly Promoted Water Oxidation of NiFe-**
2   **Layered Double Hydroxide**
3
4   *Mengjie Liu, Kyung-Ah Min, Byungchan Han,* and Lawrence Yoon Suk Lee**
5

6   Mengjie Liu, Prof. Lawrence Yoon Suk Lee
7   Department of Applied Biology and Chemical Technology and the State Key Laboratory of
8   Chemical Biology and Drug Discovery, The Hong Kong Polytechnic University, Hung Hom,
9   Kowloon, Hong Kong SAR, China
10   E-mail: lawrence.ys.lee@polyu.edu.hk
11
12   Prof. Lawrence Yoon Suk Lee
13   Research Institute for Smart Energy, The Hong Kong Polytechnic University, Hung Hom,
14   Kowloon, Hong Kong SAR, China
15
16   Dr. Kyung-Ah Min, Prof. Byungchan Han
17   Department of Chemical and Biomolecular Engineering, Yonsei University, Seoul, Republic of
18   Korea
19   E-mail: bchan@yonsei.ac.kr
20

21   Keywords: NiFe-LDH, transition metal doping, interface engineering, oxygen evolution
22   reaction, cerium hydroxide nanoparticles
23

Abstract:

Surface engineering of transition metal layered double hydroxides (LDHs) provides an efficient way of enhancing their catalytic activity toward oxygen evolution reaction (OER). However, the underlying mechanism of atomistic doping or heterogeneous interface with foreign atom is still ambiguous. Herein, we report a case study of NiFe-LDHs that are homogeneously doped with Ce (CeNiFe-LDH) and interfaced with $Ce(OH)_3$ (Ce@NiFe-LDH), which elucidates their electronic modulation, *in situ* evolution of active site, and catalytic reaction mechanisms by using X-ray photoelectronic spectroscopy, *operando* electrochemical Raman spectroscopy, and first-principles density functional theory (DFT) calculations. Our results indicate that Ce and Fe atoms serve as the electron acceptors and facilitate the coupled oxidation of $Ni^{3+/4+}$ in NiFe-LDH, and the activated oxyhydroxide phase of the catalysts exhibit superior catalytic activity for water oxidation. Especially, Ce@NiFe-LDH shows a stronger electron transfer between the loaded $Ce(OH)_3$ and the matrix, which leads to a better catalytic activity than CeNiFe-LDH. DFT calculations provide a clear picture with atomistic resolution for charge redistribution in the NiFe-LDH surface induced by Ce, which eventually leads to the optimal free energy landscape for the enhanced OER catalytic activity.

1. Introduction

Rapidly increasing global consumption of fossil fuel has inevitably raised the concerns about energy shortage and environmental degradation. To cope with these problems simultaneously, extensive effort has been devoted on the development of efficient and cost-effective renewable energy conversion and storage technologies, such as electrochemical water splitting and metal-air batteries.[1] Oxygen evolution reaction (OER) that takes place at the anodes of such applications is recognized as the bottleneck of device efficiency due to its sluggish kinetics, and it usually requires efficient yet costly precious metal oxides, such as RuO_2 and IrO_2, to overcome high overpotential barrier.[2] The sluggish kinetics of OER process stems from the four elementary steps involving multi-electron transfer, in which undesirable free energy landscape of intermediates such as *OH and *OOH accounts for the major energy and efficiency losses.[3] [2c] Considering the high costs and well-known poisoning issues of noble metallic catalysts, it is of great importance to develop high-performance electrocatalysts based on earth-abundant elements.

NiFe layered double (oxy)hydroxides (NiFe-LDHs, $[Ni_{1-x}Fe_x(OH)_2](A^{n-})_{x/n}\cdot mH_2O$), are among the most active and stable electrocatalysts for OER under alkaline conditions,[4] of which performances surpass those of Ru/Ir-based benchmark electrocatalysts, perovskite oxides,[5] spinel oxides,[6] and other transition metal-based catalysts.[7] As a relatively new member of 2D materials family, the NiFe-LDHs consist of edge-shared nickel/iron oxide octahedra layers and charge-balancing interlayer anions.[8] The substituted Fe^{3+} ions were reported to promote the OER activity of single metal (oxy)hydroxides/oxides, although its role in the OER elementary steps and synergistic mechanism are still under debate.[4a, 4b, 9] Generally, Fe^{3+} species is believed to play important roles in regulating the electronic structure,[10] reconstructing the surface energy,[11] and weakening *OH adsorption on the NiFe-LDHs.[12]

Among various attempts made to explore catalytic OER mechanism and thereby enhance performance, the incorporation of foreign elements such as cerium, vanadium, and cobalt was

1   effective in modifying the electronic structure and charge density of NiFe-LDHs, which led to

2   favorable binding energies for the intermediates.[13] Such incorporations of foreign species were

3   achieved by either doping them into the LDH lattice to form ternary hydroxides,[13c, 13e, 13f, 14] or

4   creating the interfaces with them to form surface-loaded hybrids.[13b, 13d, 15] The doping of

5   foreign metals was shown to be potent in modulating the electronic structure of LDHs without

6   creating any undesired phase segregation.[13f] On the other hand, the surface-loaded metal

7   hybrids were claimed to create an interface that could adjust the atomic configuration and/or

8   charge distribution of host metal sites. Moreover, the multifunctional hybrids on the interface

9   may serve as a hydrogen acceptor and thus optimize the adsorption behaviors to break the OH*–

10   OOH* scaling relationship in OER.[4g, 13d, 15b, 15c, 16] To the best of our knowledge, the impacts of

11   these two types of NiFe-LDH modification on OER activity have not been systematically

12   compared. The electrochemical spectroscopic information on the pre-catalytic and activated

13   states of modified NiFe-LDHs would offer in-depth insights into the structure of active site–

14   OER activity relationship.

15   In this work, both hybrid Ce(OH)$_3$ nanoparticle-deposited NiFe-LDH (Ce@NiFe-LDH) and

16   Ce-doped NiFe-LDH (CeNiFe-LDH) nanosheet arrays were synthesized and their

17   electrocatalytic OER performances were compared. X-ray photoelectron spectroscopic (XPS)

18   data indicate that the electronic structures of Ce@NiFe-LDH and CeNiFe-LDH are modulated

19   at different levels, which is consistent with density functional theory (DFT) calculations. Based

20   on systematic *operando* Raman studies, we reveal that the introduction of Ce facilitates the

21   oxidation of Ni^{3+} to Ni^{4+} *via* charge redistribution on the surface. The new charge profile leads

22   to enhanced OER catalytic performance *via* optimized binding energies of the reaction

23   intermediates on the two Ce-modified NiFe-LDH catalysts.

24   **2. Results and Discussion**

25   **2.1. Fabrication and Characterization of Catalysts**

26   **Figure 1** illustrates the synthetic procedures for NiFe-layered double hydroxide (NiFe-LDH),

4

Ce(OH)$_3$ nanoparticle-deposited NiFe-LDH (Ce@NiFe-LDH), and Ce-doped NiFe-LDH (CeNiFe-LDH) nanosheet arrays (NSAs) grown on Ni foam under hydrothermal conditions. For homogeneous distribution of Ce atoms, the CeNiFe-LDH NSAs were prepared *via* one-pot synthetic method, whereas the Ce@NiFe-LDH NSAs were fabricated in two steps to deposit Ce(OH)$_3$ nanoparticles on the surface of NiFe-LDH, creating interfaces between two phases. For comparison, Ni(OH)$_2$ NSAs were also prepared on a Ni foam using only Ni precursor (**Figure S1**).

The scanning electron microscopic (SEM) images of Ce@NiFe-LDH and CeNiFe-LDH (**Figure 2a** and **2e**) display a similar nanosheet morphology of uniform thickness (*ca*. 10 nm), which are vertically and densely grown on a Ni foam. High-resolution SEM images (insets in **Figure 2a** and **2e**), however, reveal the contrasting surface morphologies of the two samples. The CeNiFe-LDH shows the stacked nanosheet layers of smooth surface, whereas the surface of Ce@NiFe-LDH is decorated with numerous nanoparticles. The transmission electron microscopic (TEM) image of Ce@NiFe-LDH (**Figure 2b**) confirms that each nanosheet of Ce@NiFe-LDH (average size = 300×600 nm^2) is loaded with a large number of Ce(OH)$_3$ nanoparticles (average d = *ca*. 7 nm) without obvious aggregation (**Figure S2**). The corresponding selected area electron diffraction (SAED) pattern (inset in **Figure 2b**) can be indexed to the (101) and (110) lattice planes of Ce(OH)$_3$ and NiFe-LDH, respectively. Clear lattice fringes with the interplanar spacings of 2.60 and 3.14 Å are observed from the high-resolution TEM (HRTEM) image (**Figure 2c**), which are assigned to the (101) and (012) planes of Ce(OH)$_3$ and NiFe-LDH, respectively. To the contrary, the TEM image of CeNiFe-LDH displays a smooth layered nanosheet morphology (**Figure 2f**) with an interplanar spacing of 2.62 Å attributed to the (012) plane of NiFe-LDH (**Figure 2g**). High-angle annular dark-field (HAADF) scanning TEM images and the corresponding element mappings of both samples (**Figure 2d** and **2h**) indicate that Ni and Fe atoms are evenly dispersed on the nanosheet. However, Ce atoms are found concentrated on the particles in Ce@NiFe-LDH, whereas they

1 are spread over the entire CeNiFe-LDH nanosheet. The Ni:Fe:Ce atomic ratios determined by

2 inductively coupled plasma optical emission spectroscopy (ICP-OES) are 6.6:1.6:1 for

3 Ce@NiFe-LDH and 10.2:1.8:1 for CeNiFe-LDH (**Table S1**). Despite the clear difference in the

4 atomic ratio, the atomic percentages of Ce in both samples are comparable, which allows fair

5 comparison of their impacts on the catalytic activity of NiFe-LDH. Two control samples, NiFe-

6 LDH and $Ni(OH)_2$, exhibit a similar structure and morphology to that of CeNiFe-LDH (**Figure**

7 **S3**). The lattice spacing of *ca*. 2.60 Å in their HRTEM images (**Figure S3c** and **S3g**) can be

8 assigned to the (012) plane of either NiFe-LDH or $Ni(OH)_2$ owing to similar crystalline

9 structures.

10 X-ray diffraction (XRD) patterns shown in **Figure 3a** indicate that all samples are

11 isostructural to α-$Ni(OH)_2$ (JCPDS No. 38-0715). An additional peak appeared at 28.3° in

12 Ce@NiFe-LDH can be attributed to the (101) facet of $Ce(OH)_3$ (JCPDS No. 19-0284), which

13 confirms the coexistence of $Ce(OH)_3$ and NiFe-LDH. Both CeNiFe-LDH and NiFe-LDH

14 exhibit no other crystalline phase, indicating that metal atoms are homogeneously distributed

15 in the crystal structure of α-$Ni(OH)_2$. It is worth noting that the peak for the (003) plane of α-

16 $Ni(OH)_2$ slightly shifts from 11.38° to 11.44° (NiFe-LDH) and 11.50° (CeNiFe-LDH and

17 Ce@NiFe-LDH), which suggests a small lattice contraction caused by the substitution of Ni

18 atoms with Fe and Ce atoms.[8a, 17]

19 **2.2. Atomic Structure and Electronic Interaction**

20 X-ray photoelectron spectroscopy (XPS) was engaged to compare the surface chemical states

21 of Ce@NiFe-LDH and CeNiFe-LDH with NiFe-LDH. The survey XPS spectra of Ce@NiFe-

22 LDH, CeNiFe-LDH, and NiFe-LDH (**Figure S4**) identify Ni, Fe, Ce, C, and O atoms without

23 any other impurities. The Ni $2p$ spectrum of NiFe-LDH exhibits two peaks at 856.1 and 873.9

24 eV with the satellites at 862.1 and 880.0 eV, an indicative of Ni in the +2 oxidation state (**Figure**

25 **3b** and **S5**). The Ni $2p_{3/2}$ and $2p_{1/2}$ peaks of Ce@NiFe-LDH show apparent shifts toward the

higher binding energies by 0.4 and 0.3 eV, respectively, compared with those of NiFe-LDH. The opposite peak shifts are observed in the Fe $2p$ region of Ce@NiFe-LDH (**Figure 3c**). The Fe $2p_{3/2}$ and Fe $2p_{1/2}$ peaks of NiFe-LDH at 714.0 and 724.5 eV confirm the presence of Fe^{3+} species, which are shifted to the lower binding energies of 713.5 and 724.4 eV in Ce@NiFe-LDH, respectively. These concomitant opposite peak shifts in Ni $2p$ and Fe $2p$ spectra imply that there is a partial electron transfer from Ni to Fe sites when Ce atoms are introduced to Ce@NiFe-LDH forming an interface. Similar peak shifts also occur in CeNiFe-LDH, yet with a smaller extent, indicating relatively weak electronic interactions compared with those in Ce@NiFe-LDH.

Figure 3d compares the Ce $3d$ spectra of Ce@NiFe-LDH, CeNiFe-LDH, and $Ce(OH)_3$, which can be deconvoluted to two sets of Ce $3d_{3/2}$ and Ce $3d_{5/2}$ peaks, and each set can be assigned to two Ce^{3+} peaks (yellow and red) and three Ce^{4+} peaks (green and blue, see **Table S2** for details).[18] The amounts of Ce^{4+} species in Ce@NiFe-LDH and CeNiFe-LDH are much lower than that in $Ce(OH)_3$, as manifested by the suppressed peak intensity of characteristic Ce^{4+} peak at 916 eV. The analysis of peak area (**Table S3**) indicates that the Ce^{3+}/Ce^{4+} ratios in Ce@NiFe-LDH (0.67) and CeNiFe-LDH (0.92) are higher than that of $Ce(OH)_3$ (0.59). The introduced Ce atoms, regardless as an interface hybrid or homogeneous dopant, act as an electron-accepting site, and hence the partial electron transfers from Ni to Fe and Ce atoms occur through the bridging O atoms in Ce@NiFe-LDH and CeNiFe-LDH, as illustrated in the schematics in **Figure 3e**. For the case of NiFe-LDH, the Ni–O–Fe unit is used to explain the charge transfer process. The π-symmetry d-orbitals (t_{2g}) of Ni^{2+} is fully occupied, causing a major electron–electron repulsion between Ni^{2+} and O^{2-}.[19] Meanwhile, there is a half occupancy in t_{2g} d-orbitals of Fe^{3+}, and a relatively weak π-donation through Fe–O bridge is generated after the coupling between Ni and Fe cations, which triggers the partial charge transfer from Ni to Fe.[9b, 13f] Considering homogenously doped Ce in the CeNiFe-LDH lattice and $Ce(OH)_3$ particles coated on the NiFe-LDH surface of Ce@NiFe-LDH, a Ni–O–Fe–O–Ce

7

1 unit is taken into consideration for the two Ce-modified samples. The electron-deficient d-

2 orbitals of Ce^{3+} compared with those of Ni^{2+} and Fe^{3+} strengthen the electron donation from the

3 lone pairs of O^{2-} to Ce^{3+}, which can alter the electronic structure of metal ions *via* strong

4 electronic interplay and influence the OER activity of these trimetallic (oxy)hydroxides.

5 **2.3. Electrocatalytic OER Performance**

6 To demonstrate the effects of electronic structure alterations, the electrochemical OER

7 performances of the as-prepared samples were compared by conducting linear sweep

8 voltammetry (LSV) in 1 M KOH saturated with O_2 at a scan rate of 0.5 mV s^{-1} (**Figure 4a**).

9 The electrolyte is of high purity and ICP-OES detects only trace amount of Fe (< 0.01 ppm).

10 Both Ce@NiFe-LDH and CeNiFe-LDH show superior OER activities compared with NiFe-

11 LDH, which indicates that the introduced Ce atoms exert positive effects on OER catalysis. In

12 particular, the Ce@NiFe-LDH achieves the best OER performance with an overpotential of

13 merely 205 and 257 mV at the current densities of 10 and 100 mA cm^{-2}, respectively. The

14 Ce@NiFe-LDH, with such low overpotentials, outperforms most of state-of-the-art OER

15 electrocatalysts based on transition metal (oxy)hydroxides (**Table S4**). The CeNiFe-LDH also

16 demonstrates good OER performances with an overpotential of 229 mV at the current density

17 of 10 mA cm^{-2}, which is lower than those required by NiFe-LDH (246 mV) and Ni $(OH)_2$ (339

18 mV). The corresponding Tafel plots of catalysts are shown in **Figure 4b** to compare their

19 catalytic kinetics. The Tafel slopes of Ce@NiFe-LDH and CeFeNi-LDH are 40.1 and 37.9 mV

20 dec^{-1}, respectively, which are similar to that of NiFe-LDH (36.9 mV dec^{-1}). These small values

21 of Tafel slopes imply fast electron transfer kinetics compared with $Ni(OH)_2$ (67.7 mV dec^{-1}),

22 confirming that the presence of Fe and Ce increases the carrier concentration and enhances the

23 conductivity of Ni (oxy)hydroxide.

24   The intrinsic catalytic activity and number of active sites are two important criteria in

25 evaluating electrocatalysts. The electrochemical active surface areas (ECSAs) of the as-

26 prepared catalysts were evaluated to investigate the specific catalytic activity by measuring the

8

electrochemical double-layer capacitance (C_{dl}) in a non-Faradaic region at various scan rates

(**Figure S6**). By plotting the current density against scan rate, the C_{dl} of Ce@NiFe-LDH,

CeNiFe-LDH, NiFe-LDH, and Ni(OH)$_2$ are determined as 1.52, 1.41, 1.15, and 1.18 mF cm$^{-2}_{geo}$,

respectively. Assuming the specific capacitance of 0.04 mF cm^{-2} for an ideal flat surface,[20] the

Ce@NiFe-LDH yields the largest ECSA of 38.0 cm$^{-2}_{ECSA}$ compared with CeNiFe-LDH (35.3

cm$^{-2}_{ECSA}$), NiFe-LDH (28.8 cm$^{-2}_{ECSA}$), and Ni(OH)$_2$ (29.5 cm$^{-2}_{ECSA}$). The largest ECSA of

Ce@NiFe-LDH can be attributed to its hierarchical structure that exposes the extended solid–

liquid interface. **Figure 4c** compares the intrinsic electrochemical activities of the as-prepared

catalysts using the ECSA-normalized current density at an operation potential of 1.5 V. The

Ce@NiFe-LDH displays a remarkably enhanced catalytic activity as manifested by a high

current density of 2.497 mA cm$^{-2}_{ECSA}$ that is almost two-fold enhancement from that of CeNiFe-

LDH (and three-fold from that of NiFe-LDH).

Turnover frequency (TOF) can be used to examine the intrinsic activity of electrocatalysts

more accurately when their active sites are well defined. It is, however, usually difficult to

determine the active sites in composite catalysts comprised of multiple metal sites due to the

lack of reliable techniques. One widely accepted method is to consider all metal sites as active

sites although it would yield an underestimated TOF value.[21] Based on the number of Ni, Fe,

and Ce sites measured by ICP-OES (**Table S1**), the TOF values of catalysts were estimated and

compared in **Figure 4d**. Similar to the ECSA-normalized current density, the Ce@NiFe-LDH

exhibits a much higher TOF of 0.084 s^{-1} compared with CeNiFe-LDH (0.038 s^{-1}), NiFe-LDH

(0.019 s^{-1}), and Ni(OH)$_2$ (0.0007 s^{-1}). These results strongly suggest that the introduction of Ce

atoms by interface engineering is a much more efficient way than simple doping for improving

the intrinsic OER activity of NiFe-LDH.

The kinetic barriers of OER process can be altered by modulating the structure of active

sites on electrocatalyst surface. By plotting Napierian logarithm of kinetic current density

against the reciprocal of temperature, the electrochemical activation energies for the as-

1   prepared catalysts were extracted from the Arrhenius plots as slopes (**Figure 4e**, see the

2   Supporting Information for details).[2a, 22] The lowest barrier energy of Ce@NiFe-LDH (27.6 kJ

3   mol^{-1}) indicates that its intrinsic catalytic activity is largely enhanced compared with those of

4   Ni(OH)$_2$ (61.2 kJ mol^{-1}) and NiFe-LDH (32.2 kJ mol^{-1}). The CeNiFe-LDH exhibits a slightly

5   higher barrier energy (29.3 kJ mol^{-1}) than Ce@NiFe-LDH, indicating that its catalytic activity

6   is also improved by Ce doping.

7   Electrochemical impedance spectroscopy (EIS) was employed to estimate the conductivity

8   of the as-synthesized catalysts. The Nyquist plots shown in **Figure 4f** were fitted by a simplified

9   Randles equivalent circuit. The radii of semicircles indicate that the charge transfer resistances

10 at the electrode/electrolyte interface of Ce@NiFe-LDH, CeNiFe-LDH, NiFe-LDH, and

11 Ni(OH)$_2$ are 0.96, 1.03, 1.08, and 25.86 Ω, respectively. The NiFe-LDH is known to possess an

12 extraordinary conductivity among Ni-based hydroxides.[4e] The incorporation of Ce(OH)$_3$

13 nanoparticles and Ce doping onto NiFe-LDH produce an optimized e_g electron filling status,

14 which further augments the charge transfer rate between the catalytic sites and oxygen-

15 containing adsorbates,[23] making a critical contribution to OER activity.

16   The associated Faradaic efficiency of Ce@NiFe-LDH was measured from a 1-h reaction at

17 an overpotential of 300 mV (**Figure 4g**). The measured O$_2$ yield closely matches the theoretical

18 yield, indicating a high energy-conversion rate (~100 %) of Ce@NiFe-LDH. Moreover, the

19 long-term stability of Ce@NiFe-LDH under OER operation conditions was evaluated by

20 chronopotentiometry. Under a steady applied potential of 1.53 V for 48 h, the Ce@NiFe-LDH

21 initial displays slightly increasing current density due to the activation process of metal ions

22 from low- to high-valance state, followed by a stabilized current density (**Figure S12**). The

23 OER polarization curve measured after the 48-h chronopotentiometric test shows almost no

24 change from the initial one, indicating the robust durability of Ce@NiFe-LDH under alkaline

25 OER conditions (**Figure 4h**). The morphology, crystal structure, and surface chemical states of

26 Ce@NiFe-LDH were characterized again after the long-term OER test by SEM, XRD, and XPS

1　(**Figure S13 – S15**). The surface morphology and structure of Ce@NiFe-LDH show no

2　detectable changes, except for *in situ* produced high valent metal species, confirming its

3　electrochemical stability in alkaline media.

4　**2.4. *Operando* Raman Spectroelectrochemistry: Activity Origin and Structural Evolution**

5　Although the electrochemical analyses clearly demonstrated excellent OER activity of

6　Ce@NiFe-LDH enabled by the incorporation of $Ce(OH)_3$ nanoparticles, several important

7　questions still remain. Is the structure of Ni or Fe components affected at the interface with Ce?

8　Which metal site serves as an active site for catalyzing OER? How does the modified active

9　site accelerate OER kinetics? To address these critical questions, *operando* Raman–

10　electrochemical investigations were first conducted on two control samples, $Ni(OH)_2$ and NiFe-

11　LDH, to investigate the states of surface metal species and structural transitions during OER

12　process (**Figure S17**).

13　　**Figure 5a** shows the Raman spectra of $Ni(OH)_2$ collected during the potential sweep from

14　1.1 to 1.625 V. At 1.1 V, two peaks corresponding to α-$Ni(OH)_2$ are observed at 459 and 497

15　cm^{-1}, which is consistent with the XRD observation. With a slight increase of potential to 1.350

16　V, two new peaks emerge at 475 and 557 cm^{-1} with a I_{557}/I_{475} intensity ratio of 1.76 (peak

17　fittings in **Figure S16**), which are assigned to the γ-NiOOH phase.[24] These Raman peaks can

18　be correlated with the first oxidation process at 1.355 V in the corresponding LSV curve (peak

19　I, **Figure 5b**). The β-NiOOH phase may appear at the same wavenumbers due to their similar

20　structure, but it shows a significantly higher I_{557}/I_{475} ratio that of γ-phase.[9a, 25] With the applied

21　potentials ≥1.375 V, the peak at 557 cm^{-1} intensifies gradually, which indicates that the β-

22　NiOOH phase starts to appear and dominates at high anodic potentials,[25] as confirmed by the

23　second oxidation peak at 1.387 V in the LSV (peak II, **Figure 5b**). The I_{557}/I_{475} ratio increases

24　to 2.19 at 1.475 V, clearly distinguishing it from the γ-phase.

25　　The Ni^{3+} species in of β/γ-NiOOH is further oxidized to Ni^{4+} *via* successive deprotonation

26　and coupled with the subsequent OER process.[26] A weak anodic signal (peak III, **Figure 5b**)

observed at 1.575 V in the LSV can be correlated to the conversion of γ-NiOOH to Ni^{4+}.[9a] However, the Ni^{4+} species transformed from inactive β-NiOOH is not observed in the LSV (usually observed at ≥ 1.620 V),[4e] most probably due to the interference from OER signal. Once passed the OER potential of 1.6 V, the Raman peaks of NiO_x appear at 468, 530, and 551 cm^{-1} and persist even at 1.625 V, while all the NiOOH peaks diminish. The intensities of these peaks are noticeably decreased due to the disappearance of resonance enhancement of NiOOH and the interference of oxygen bubbles.[25] Pristine $Ni(OH)_2$/NiOOH is usually recognized as a poor OER catalyst,[27] which requires a large external energy to generate the active Ni^{4+} species before the onset of OER (1.58 V in **Figure 5b**).

An *operando* Raman analysis of NiFe-LDH is shown in **Figure 5c**. At the open circuit potential, two characteristic broad peaks of defective or disordered $Ni^{2+}Fe^{3+}$-LDH are visible at 461 and 530 cm^{-1}. A new broad shoulder at 557 cm^{-1} is assigned to NiOOH, which intensifies as the potential is increased to 1.475 V. The corresponding LSV shows a $Ni(OH)_2$/NiOOH anodic wave that is positively shifted to 1.400 V. This observation indicates that the presence of Fe shifts the Ni^{2+}/Ni^{3+} oxidation to a higher potential, lowering the valence state of Ni sites.[4b, 4d, 9b, 28] At 1.5 V, new peaks corresponding to high valent NiO_x appear as shoulders at 468 and 551 cm^{-1} and then gradually dominate at higher OER potentials (≥ 1.525 V). This transition takes place at a much lower potential (1.500 V) compared with the case of $Ni(OH)_2$ (1.600 V), which suggests that the Ni^{3+} to Ni^{4+} oxidation is accelerated by the presence of Fe^{3+} species. The corresponding electrochemical signal is merged with OER catalytic current due to the enhanced performance of NiFe-LDH.[27] It was reported that Fe^{3+} can serve as a Lewis acid and increase the acidity of OH_x moieties coordinated to Ni site, thus lowering the reduction potential of $Ni^{3+/4+}$ couple.[29] Such quick conversion of Ni^{3+} to Ni^{4+} is believed to lead to the facilitated OER process.[27]

It is clear that $Ni(OH)_2$ and NiFe-LDH undergo different transformation pathways under applied anodic potentials. The Fe^{3+} species in NiFe-LDH plays the key role in facilitating the

1   oxidation of Ni^{3+} to Ni^{4+} at a much lower potential,[29] which results in the boost of subsequent

2   OER kinetics. The presence and role of Fe^{4+} in NiFe hydroxides during OER still remain a

3   controversial topic.[9b, 30], [27] Although the Raman spectra could not detect the transition of Fe^{3+}

4   to Fe^{4+} in our case, the role of high valent Fe species cannot be completely ruled out. Here, the

5   active site for OER is described as $Ni^{3+}OOH$ and its oxidized Ni^{4+} state.[4b, 26, 29]

6   With the information on the structural evolution of $Ni(OH)_2$ and NiFe-LDH, the phase

7   transition and active sites in CeNiFe-LDH and Ce@NiFe-LDH were investigated using the

8   electrochemical Raman spectroscopy. Both CeNiFe-LDH and Ce@NiFe-LDH display a similar

9   phase transition in Raman spectra and voltammetric responses as NiFe-LDH (**Figure 6**),

10   suggesting that main OER active species remains the same. At the open circuit potential, typical

11   broad peaks of $Ni(OH)_2$ (497 cm^{-1}) and NiFe-LDH (461 and 530 cm^{-1}) are observed from both

12   samples without any features of NiOOH species. At an applied potential of 1.450 V, however,

13   CeNiFe-LDH shows a NiOOH peak at 557 cm^{-1}, an indicative of the $Ni^{2+/3+}$ oxidization (**Figure**

14   **6a**). As the potential is increased to 1.475 V, the NiOOH peak intensifies and a broad peak

15   emerges at 468 cm^{-1}, which may be attributed to NiO_x. This high valent NiO_x peak persists at

16   1.550 V as confirmed by dominant peaks at 468, 530, and 551 cm^{-1}, serving as the active site

17   for OER. The corresponding LSV detects only one broad anodic peak at 1.375 V, which is

18   attributed to γ- or β-NiOOH species (**Figure 6b**).

19   **Figure 6c** shows the *operando* Raman spectra of Ce@NiFe-LDH that undergoes almost

20   identical transition process as CeNiFe-LDH, however, at lower potentials (by 25 and 50 mV

21   than CeNiFe-LDH and NiFe-LDH, respectively). These results clearly indicate that NiFe-LDH,

22   CeNiFe-LDH, and Ce@NiFe-LDH undergo the same structural evolution and share the

23   identical catalytic sites. Interestingly, no obvious anodic peak is observed in the corresponding

24   LSV curve, probably due to earlier start of OER process. With the earlier transition to the active

25   phase, the Ce@NiFe-LDH apparently shows a higher OER activity. The activity trend can be

26   further confirmed by the onset potentials of OER process: 1.42 V for Ce@NiFe-LDH, 1.45 V

1   for CeNiFe-LDH, and 1.48 V for NiFe-LDH. Such a trend, consistent with the Ni oxidation

2   potential, indicates that the activation of Ni site should be responsible for the subsequent OER.

3   The introduction of Ce, by either doping or interface engineering, was demonstrated to facilitate

4   the oxidation of Ni^{3+} to Ni^{4+} and thus decrease the onset potential of OER. The high valent Ce

5   species are speculated to serve as a Lewis acid just as Fe^{3+},[29] increase the acidity of OH_x

6   moieties coordinated to Ni site, thus lowering the redox potential of $Ni^{3+/4+}$. However, the

7   elucidation of kinetics and reaction pathways still require the atomic-level interpretations.

8   **2.5. First-principles Density Functional Theory Calculations**

9   To reveal the underlying mechanism of high OER catalytic performance of Ce@NiFe-LDH,

10   the first-principles density functional theory (DFT) calculations were carried out. It was

11   reported that the overpotential for OER is independent of NiOOH facets,[31] thus the Ni-

12   terminated (110) plane with the lowest surface energy was considered as the computational

13   model, where OER intermediates can directly react with metal sites on the undercoordinated

14   facet (**Figure S18**). To elucidate the influence of Ce on the OER catalysis of NiFe-LDH, the

15   charge density changes of CeNiFe-LDH and Ce@NiFe-LDH were calculated in the Ce-

16   substituted and $Ce(OH)_3$-loaded LDH slabs. **Figure 7a** represents the charge density difference

17   between NiFe-LDH and CeNiFe-LDH (or Ce@NiFe-LDH). The charge redistribution in the

18   CeNiFe-LDH can be ascribed to the doped Ce atoms that have different charge densities from

19   original Ni or Fe atoms in NiFe-LDH, while in the Ce@NiFe-LDH, it was caused by electron

20   transfer between $Ce(OH)_3$ and NiFe-LDH. Such subtle different features in charge

21   configuration have effect on the adsorption strength of OER intermediates onto the LDH, which

22   essentially modulates the rate-determining step (RDS).

23   We calculated the Gibbs free energies of OH*, O*, and OOH* intermediates along the

24   elementary pathway on NiFe-LDH, CeNiFe-LDH, and Ce@NiFe-LDH at $U = 1.23$ V (**Figure**

25   **7b**). Free energy diagrams at different potentials for three models are provided in **Figure S19**–

26   **S21**. The OH*, O*, and OOH* are preferentially adsorbed on the Ni-sites of NiFe-LDH,

CeNiFe-LDH, and Ce@NiFe-LDH (110) surfaces. In **Figure 7b**, the RDS is determined to be the second step from OH* to O* on NiFe-LDH and Ce@NiFe-LDH with the largest free energy differences. However, it becomes the fourth step from OOH* to O_2 (*g*) for CeNiFe-LDH. The differences are attributed to the dissimilar surface charge configuration between CeNiFe-LDH and Ce@NiFe-LDH. **Figure 7c** compares the free energy difference among three models at RDS. It is noteworthy that the incorporation of foreign element Ce remarkably reduces energy barrier for climbing the RDS from 0.92 eV (NiFe-LDH) to 0.61 eV (CeNiFe-LDH) or 0.56 eV (Ce@NiFe-LDH). Furthermore, we reveal that doped Fe also regulates the adsorption strengths of OH* and O* intermediates, which enhances the OER activity of LDHs compared to the pristine $Ni(OH)_2$ with the activation energy barrier of 1.13 eV (**Figure S22**). The theoretical trend is very consistent with the experimental measurements shown in **Figure 4a**. To sum up, the incorporation of Ce in NiFe-LDH optimally modulate the adsorption free energy landscape of OH*, O*, and OOH* intermediates, leading to enhanced OER catalysis on both of the CeNiFe-LDH and Ce@NiFe-LDH.

3. Conclusion

In summary, two types of Ce-modified NiFe-LDH catalysts, heterogenous Ce@NiFe-LDH and ternary CeNiFe-LDH, were prepared and their OER activities were investigated with respect to NiFe-LDH and $Ni(OH)_2$. Electronic structure and coordination chemistry were substantially modulated by the interface engineering and doping, leading to the enhanced intrinsic catalytic activity and boosting up of the water oxidation performance in alkaline electrolyte. Remarkably, the Ce@NiFe-LDH with abundant interfaces displays superior charge transfer ability and catalytic activity with an overpotential of 205 mV at the current density of 10 mA cm^{-2}. A high current density (up to 65 mA cm^{-2}) can be maintained stably for 48 h. The systematic *operando* Raman characterizations unveiled the structural evolution from the pre-catalytic state to the activated state during OER process, demonstrating that Fe and Ce can facilitate the $Ni^{3+/4+}$

15

coupled oxidation and further decrease the overpotential of subsequent water oxidation. Theoretical calculations verify the dissimilar charge redistribution in NiFe-LDH by doped Ce atoms or loaded hybrids, which leads to the optimal adsorption free energy landscape of OER intermediates accounting for enhanced catalytic activity. These findings provide insights into atomic-scale mechanism and surface engineering for enhancing the OER activity of NiFe oxyhydroxides *via* incorporation of heteroatoms or nanoparticles. It should be certainly useful for the interface engineering and homogenous atomic dispersion as a mean of tuning the physiochemical proprieties of transition metal oxyhydroxides to boost their catalytic activity.

4. Experimental Section/Methods

Chemicals:

Nickel(II) nitrate hexahydrate ($Ni(NO_3)_2 \cdot 6H_2O$, 99.9%), iron(III) nitrate nonahydrate ($Fe(NO_3)_3 \cdot 9H_2O$, 99.9%), cerium(III) chloride heptahydrate ($CeCl_3 \cdot 7H_2O$, 99.9%), urea ($CO(NH_2)_2$, >98%), ammonium fluoride (NH_4F, > 98%), and potassium hydroxide (KOH, 99.99%) were purchased from Sigma–Aldrich, USA. Hydrochloric acid (HCl, 37%) and nitric acid (HNO_3, 68%) were purchased from Duksan Co., Korea. All chemicals were used as received. All solutions were prepared using deionized (DI) Milli-Q water (15 MΩ cm^{-1} at 25 °C).

Materials Synthesis:

Synthesis of $Ni(OH)_2$ and NiFe Layered Double Hydroxide Nanosheet Arrays: For the synthesis of $Ni(OH)_2$ nanosheet arrays (NSAs), Ni foam was first cut into a rectangle (3×2 cm^2) and corroded in 10 % HCl for 10 min to remove surface oxide species, followed by washing with DI water for 10 min. This pre-cleaned Ni foam was vertically immersed into a 80 mL Teflon autoclave vessel filled with a solution (67 mL) containing $Ni(NO_3)_2 \cdot 6H_2O$ (1.454 g, 5 mmol), NH_4F (0.370 g, 10 mmol), and $CO(NH)_2$ (1.451 g, 25 mmol) and heated to 120 °C for 8 h. After cooled down to room temperature, the product was collected by filtration and washed with DI water multiple times. For the synthesis of NiFe-LDH NSAs, the same protocol was used except

16

that $Ni(NO_3)_2 \cdot 6H_2O$ was replaced with a 4:1 mixture of $Ni(NO_3)_2 \cdot 6H_2O$ (1.163 g, 4 mmol) and

$Fe(NO_3)_3$ $9H_2O$ (0.404 g, 1 mmol).

Synthesis of CeNiFe-LDH and Ce@NiFe-LDH Nanosheet Arrays: NiFe-LDH NSAs

homogeniously doped with Ce atoms (CeNiFe-LDH) were prepared by one-step method using

the same procedure for the NiFe-LDH NSAs except that $CeCl_3 \cdot 7H_2O$ (0.373 g, 1 mmol) was

also added to the reaction mixture. NiFe-LDH NSAs heterogeneously loaded with $Ce(OH)_3$

nanoparticles (Ce@NiFe-LDH) were fabricated by two-step method in a weak alkaline medium

to avoid Ce doping *via* ionic exchange and/or etching process. The as-prepared NiFe-LDH

NSAs on Ni foam was immersed vertically into 67 mL of mixture solution containing 1 mmol

$CeCl_3 \cdot 7H_2O$ (0.373 g), 2 mmol NH_4F (0.074 g) and 5 mmol $CO(NH_2)_2$ (0.290 g). The autoclave

was heated to 120 ℃ for 5 h.

Materials Characterizations:

Scanning electron microscopic (SEM) image was acquired using a field emission (FE) scanning

electron microscope (TESCAN MAIA3). Transmission electron microscopic (TEM) image and

elemental distribution mappings were obtained using a transmission electron microscope (JEOL

Model JEM-2100F, 200 kV) equipped with an energy dispersive spectrometer (EDS). Powder

X-ray diffraction (XRD) patterns were collected on a SmartLab X-ray diffractometer (Rigaku,

voltage = 45 kV, current = 200 mA). X-ray photoelectron spectroscopy (XPS) was conducted

on an X-ray photoelectron spectrometer (ESCALAB 250Xi, Thermo Fisher). The C 1*s* peak at

284.8 eV was used for spectrometer calibration. The XPS data were analyzed using a CasaXPS

software with a background type of Shirley and peak profile of Gaussian–Lorentzian GL(30).

The elemental compositions were determined by inductively coupled plasma optical emission

spectroscopy (ICP-OES) on an Agilent 710 Series spectrometer.

Electrochemical Measurements:

Electrochemical oxygen evolution reaction was performed in a standard three-electrode

configuration and the data were collected by a Princeton multichannel electrochemical station

1   in O_2-saturated 1 M KOH (high purity, 99.99%) at 25 °C. The as-synthesized samples on nickel

2   foam were directly used as the working electrode, and a Pt foil and Hg/HgO electrode were

3   employed as the counter and reference electrodes, respectively. All current densities were

4   calculated based on the geometrical area of electrodes and measured currents. Before each

5   electrochemical test, the working electrode was stabilized by cycling the potential from 1.025

6   to 1.525 V for 20 times at a scan rate of 50 mV s^{-1}. Linear sweep voltammograms (LSVs) were

7   obtained within the potential window between 1.0 and 1.8 V *vs.* reversible hydrogen electrode

8   (RHE) at a scan rate of 0.5 mV s^{-1}. All measurements were repeated at least three times.

9   *iR Compensation:* To compensate the *i*R drop during the LSV measurements, electrochemical

10   impedance spectra (EIS) were recorded at 1.53 V *vs.* RHE in the frequency range between 100

11   kHz and 10 mHz with the amplitude of 10 mV. All polarization curves were corrected by 90 %

12   *i*R-compensation for ohmic losses arising from active materials, substrate, and solution

13   resistances. The value of R was determined from the Z_{re}-intercept of the arc in the Nyquist plot.

14   *Electrochemical Active Surface Area:* Electrochemical active surface area (ECSA) was

15   estimated by measuring double layer capacitance (C_{dl}) from the cyclic voltammograms (CVs)

16   obtained within the non-Faradaic potential window between 1.205 and 1.265 V at various scan

17   rates (20, 40, 60, 80, and 100 mV s^{-1}). From the plot of current density (the sum of absolute

18   values of current density at 1.235 V *vs.* RHE) against the scan rate, the C_{dl} value was determined

19   as the slope of a straight line. Assuming the specific capacitance of 0.04 mF cm^{-2} for an ideal

20   flat surface, the electrochemical active surface area can be calculated by the following equation:

21   $$A_{ECSA} = \frac{C_{dl}(catalyst)}{0.04 \text{ mF·cm}^{-2}} \qquad (1)$$

22   *Turnover Frequency:* Turnover frequency (TOF) of the reaction was calculated by the following

23   equation:

24   $$TOF = \frac{j \times A_{geo}}{n \times F \times N_{site}} \qquad (2)$$

1   where j is the current density at an overpotential of 285 mV, A_{geo} is the geometric area of the

2   electrode, n is the number of electrons involved (4 for OER), F is the Faraday constant, and

3   N_{site} is the total number of metal sites (mole) on the electrode determined by ICP-OES (**Table**

4   **S1**).

5   *Faradaic Efficiency:* Faradaic efficiency (η) was calculated from the total charge passed

6   through the electrode (Q, read from the electrochemical station) and the amount of produced

7   oxygen (n_{O_2}, measured by dewatering method) using the equation.:

8 $$\eta = \frac{4F \times n_{O_2}}{Q} \qquad (3)$$

9   *Arrhenius Plots:* A sealed cell was used to minimize the evaporative of electrolyte loss in a

10   thermostatic water bath with a temperature controller. The dependence of catalytic currents on

11   the reaction temperature is shown in **Figure S7**. According to the Arrhenius relationship shown

12   below,

13 $$k = A \exp(\frac{-E_a}{RT}) \qquad (4)$$

14   the apparent electrochemical activation enthalpy (E_a) for OER was determined from the slope

15   of Arrhenius plot:

16 $$\frac{\partial(\ln i_0)}{\partial(\frac{1}{T})} = -\frac{E_a}{R} \qquad (5)$$

17   where k is the rate constant, A is the pre-exponential factor, R is the universal gas constant, T is

18   the absolute temperature, and i_0 is the kinetic current density.

19   *Operando Raman-electrochemical experiments: Operando* Raman spectroelectrochemical

20   measurements were carried out on a confocal Renishaw micro-Raman spectroscopy system

21   with a 785 nm stream-line laser excitation using a long working distance 50× magnification

22   objective lens. Each spectrum was accumulated with 10 s exposure time and 0.5% of laser

23   intensity (laser power was reduced to 1.5 mW to prevent the decomposition of sample). A

24   Hg/HgO (1.0 M KOH) electrode and a Pt wire were employed as the reference and counter

1   electrodes, respectively. CVs were obtained at a scan rate of 0.3 mV s^{-1} using high purity 1 M

2   KOH as the electrolyte. The as-prepared electrode was directly used for Raman study.

3   *First-principles Calculation:*

4   To elucidate the underlying mechanism of the enhanced OER activity in NiFe-LDHs

5   incorporated Ce, spin polarized DFT calculations were performed. The generalized gradient

6   approximation (GGA) for exchange-correlation (*xc*) functionals implemented in the Vienna *ab-*

7   *initio* simulation package (VASP) was used for the computing.[32] The projector augmented

8   wave (PAW) potentials were used to describe electron-ion interaction. Kinetic energy cut-off

9   was set to 400 eV for expanding the plane-wave basis set.[33] For van der Waals (vdW)

10   corrections, the Grimme's DFT-D3 scheme based on a semi-empirical GGA-type theory was

11   adopted.[34] The Hubbard *U* term was corrected by DFT+U calculations introduced by Dudarev

12   *et al.* with *U–J* parameters of 5.3 and 5.5 for the Fe and Ni, respectively.[35] In the calculations,

13   undercoordinated Ni-terminated NiFe-LDH(110) surfaces were chosen due to its lowest surface

14   energy. Then, Ce atoms were substitutionally doped for Fe or Ce(OH)$_3$ nanoparticle was

15   adsorbed to construct CeNiFe-LDH or Ce@NiFe-LDH, respectively (**Figure S18**). For the

16   Brillouin-zone integration in the reciprocal space, $(1 \times 3 \times 1)$ grids were utilized in the Gamma-

17   centered scheme. All model structures were fully optimized until the Hellmann-Feynman forces

18   and energies were reached to 0.04 eV Å^{-1} and 1×10^{-5} eV, respectively.

19   The charge density difference Δn_1 (or Δn_2) between NiFe-LDH and CeNiFe-LDH (or

20   Ce@NiFe-LDH) was calculated by following equation:

21          $\Delta n_1 = n_{\text{CeNiFe-LDH}} - (n_{\text{CeNiFe-LDH}} + n_{\text{Ce}} - n_{\text{Fe}})$ (6)

22          $\Delta n_2 = n_{\text{Ce@NiFe-LDH}} - (n_{\text{CeNiFe-LDH}} + n_{\text{Ce(OH)}_3})$ (7)

23   where $n_{\text{CeNiFe-LDH}}$, $n_{\text{Ce@NiFe-LDH}}$, $n_{\text{NiFe-LDH}}$, $n_{\text{Ce(OH)}_3}$ are total charge densities of NiFe-LDH,

24   CeNiFe-LDH, Ce@NiFe-LDH, and Ce(OH)$_3$, respectively, and n_{Ce} and n_{Fe} are atomic charge

25   densities of Ce and Fe atoms, respectively.

26   Gibbs free energies for OER intermediates were calculated by following equation:

$$\Delta G = \Delta E + \Delta ZPE - T\Delta S \qquad (8)$$

where ΔE is adsorption energy of OH*, O*, or OOH* intermediates on LDH, ΔZPE is the zero-point energy correction, and ΔS is the entropy change by the intermediate adsorbates.

Supporting Information
Supporting Information is available from the Wiley Online Library or from the author.

Acknowledgements

1   References

2   [1]   a) I. Roger, M. A. Shipman, M. D. Symes, *Nat. Rev. Chem.* **2017**, 1, 0003; b) F.

3   Cheng, J. Chen, *Chem. Soc. Rev.* **2012**, 41, 2172; c) Y. Li, J. Lu, *ACS Energy Lett.*

4   **2017**, 2, 1370.

5   [2]   a) B. Zhang, X. Zheng, O. Voznyy, R. Comin, M. Bajdich, M. García-Melchor, L.

6   Han, J. Xu, M. Liu, L. Zheng, F. P. García de Arquer, C. T. Dinh, F. Fan, M. Yuan, E.

7   Yassitepe, N. Chen, T. Regier, P. Liu, Y. Li, P. De Luna, A. Janmohamed, H. L. Xin,

8   H. Yang, A. Vojvodic, E. H. Sargent, *Science* **2016**, 352, 333; b) F. Dionigi, Z. Zeng,

9   I. Sinev, T. Merzdorf, S. Deshpande, M. B. Lopez, S. Kunze, I. Zegkinoglou, H.

10   Sarodnik, D. Fan, A. Bergmann, J. Drnec, J. F. d. Araujo, M. Gliech, D. Teschner, J.

11   Zhu, W.-X. Li, J. Greeley, B. R. Cuenya, P. Strasser, *Nat. Commun.* **2020**, 11, 2522; c)

12   C. C. L. McCrory, S. Jung, I. M. Ferrer, S. M. Chatman, J. C. Peters, T. F. Jaramillo,

13   *J. Am. Chem. Soc.* **2015**, 137, 4347.

14   [3]   M. J. Craig, G. Coulter, E. Dolan, J. Soriano-López, E. Mates-Torres, W. Schmitt, M.

15   García-Melchor, *Nat. Commun.* **2019**, 10, 4993.

16   [4]   a) L. Trotochaud, S. L. Young, J. K. Ranney, S. W. Boettcher, *J. Am. Chem. Soc.*

17   **2014**, 136, 6744; b) D. Friebel, M. W. Louie, M. Bajdich, K. E. Sanwald, Y. Cai, A.

18   M. Wise, M.-J. Cheng, D. Sokaras, T.-C. Weng, R. Alonso-Mori, R. C. Davis, J. R.

19   Bargar, J. K. Nørskov, A. Nilsson, A. T. Bell, *J. Am. Chem. Soc.* **2015**, 137, 1305; c)

20   F. Song, X. Hu, *Nat. Commun.* **2014**, 5, 4477; d) C. Tang, H.-F. Wang, H.-S. Wang, F.

21   Wei, Q. Zhang, *J. Mater. Chem. A* **2016**, 4, 3210; e) M. Gong, Y. Li, H. Wang, Y.

22   Liang, J. Z. Wu, J. Zhou, J. Wang, T. Regier, F. Wei, H. Dai, *J. Am. Chem. Soc.* **2013**,

23   135, 8452; f) J. Zhou, L. Yu, Q. Zhu, C. Huang, Y. Yu, *J. Mater. Chem. A* **2019**, 7,

24   18118; g) Y. Wang, P. Zheng, M. Li, Y. Li, X. Zhang, J. Chen, X. Fang, Y. Liu, X.

25   Yuan, X. Dai, H. Wang, *Nanoscale* **2020**, 12, 9669.

[5] J. T. Mefford, X. Rong, A. M. Abakumov, W. G. Hardin, S. Dai, A. M. Kolpak, K. P. Johnston, K. J. Stevenson, *Nat. Commun.* **2016**, 7, 11053.

[6] T. Maiyalagan, K. A. Jarvis, S. Therese, P. J. Ferreira, A. Manthiram, *Nat. Commun.* **2014**, 5, 3949.

[7] a) Y. Li, L. Hu, W. Zheng, X. Peng, M. Liu, P. K. Chu, L. Y. S. Lee, *Nano Energy* **2018**, 52, 360; b) E. M. Miner, M. Dincă, *Nat. Energy* **2016**, 1, 16186.

[8] a) D. Wang, Q. Li, C. Han, Q. Lu, Z. Xing, X. Yang, *Nat. Commun.* **2019**, 10, 3899; b) B. M. Hunter, W. Hieringer, J. R. Winkler, H. B. Gray, A. M. Müller, *Energy Environ. Sci.* **2016**, 9, 1734.

[9] a) S. Klaus, Y. Cai, M. W. Louie, L. Trotochaud, A. T. Bell, *J. Phys. Chem. C* **2015**, 119, 7243; b) J. Y. C. Chen, L. Dang, H. Liang, W. Bi, J. B. Gerken, S. Jin, E. E. Alp, S. S. Stahl, *J. Am. Chem. Soc.* **2015**, 137, 15090.

[10] Y. Liu, Y. Ying, L. Fei, Y. Liu, Q. Hu, G. Zhang, S. Y. Pang, W. Lu, C. L. Mak, X. Luo, L. Zhou, M. Wei, H. Huang, *J. Am. Chem. Soc.* **2019**, 141, 8136.

[11] T. Wu, S. Sun, J. Song, S. Xi, Y. Du, B. Chen, W. A. Sasangka, H. Liao, C. L. Gan, G. G. Scherer, L. Zeng, H. Wang, H. Li, A. Grimaud, Z. J. Xu, *Nat. Catal.* **2019**, 2, 763.

[12] H. B. Tao, Y. Xu, X. Huang, J. Chen, L. Pei, J. Zhang, J. G. Chen, B. Liu, *Joule* **2019**, 3, 1498.

[13] a) H. Xu, B. Wang, C. Shan, P. Xi, W. Liu, Y. Tang, *ACS Appl. Mater. Interfaces* **2018**, 10, 6336; b) X. Wang, Y. Yang, L. Diao, Y. Tang, F. He, E. Liu, C. He, C. Shi, J. Li, J. Sha, S. Ji, P. Zhang, L. Ma, N. Zhao, *ACS Appl. Mater. Interfaces* **2018**, 10, 35145; c) Y. Yang, L. N. Dang, M. J. Shearer, H. Y. Sheng, W. J. Li, J. Chen, P. Xiao, Y. H. Zhang, R. J. Hamers, S. Jin, *Adv. Energy Mater.* **2018**, 8, 1703189; d) J. Liu, J. Wang, B. Zhang, Y. Ruan, L. Lv, X. Ji, K. Xu, L. Miao, J. Jiang, *ACS Appl. Mater. Interfaces* **2017**, 9, 15364; e) Q. Q. Chen, C. C. Hou, C. J. Wang, X. Yang, R. Shi, Y.

Chen, *Chem. Commun.* **2018**, 54, 6400; f) J. Jiang, F. Sun, S. Zhou, W. Hu, H. Zhang, J. Dong, Z. Jiang, J. Zhao, J. Li, W. Yan, M. Wang, *Nat. Commun.* **2018**, 9, 2885.

[14]   Z. Lu, L. Qian, Y. Tian, Y. Li, X. Sun, X. Duan, *Chem. Commun.* **2016**, 52, 908.

[15]   a) N. H. Kwon, M. Kim, X. Jin, J. Lim, I. Y. Kim, N.-S. Lee, H. Kim, S.-J. Hwang, *NPG Asia Mater.* **2018**, 10, 659; b) J. Chen, F. Zheng, S.-J. Zhang, A. Fisher, Y. Zhou, Z. Wang, Y. Li, B.-B. Xu, J.-T. Li, S.-G. Sun, *ACS catal.* **2018**, 8, 11342; c) Z.-W. Gao, J.-Y. Liu, X.-M. Chen, X.-L. Zheng, J. Mao, H. Liu, T. Ma, L. Li, W.-C. Wang, X.-W. Du, *Adv. Mater.* **2019**, 31, 1804769.

[16]   a) J. Zhang, J. Liu, L. Xi, Y. Yu, N. Chen, S. Sun, W. Wang, K. M. Lange, B. Zhang, *J. Am. Chem. Soc.* **2018**, 140, 3876; b) J.-X. Feng, S.-H. Ye, H. Xu, Y.-X. Tong, G.-R. Li, *Adv. Mater.* **2016**, 28, 4698.

[17]   Z. Qiu, C.-W. Tai, G. A. Niklasson, T. Edvinsson, *Energy Environ. Sci.* **2019**, 12, 572.

[18]   E. Bêche, P. Charvin, D. Perarnau, S. Abanades, G. Flamant, *Surf Interface Anal.* **2008**, 40, 264.

[19]   S. Zhao, Y. Wang, J. Dong, C.-T. He, H. Yin, P. An, K. Zhao, X. Zhang, C. Gao, L. Zhang, J. Lv, J. Wang, J. Zhang, A. M. Khattak, N. A. Khan, Z. Wei, J. Zhang, S. Liu, H. Zhao, Z. Tang, *Nat. Energy* **2016**, 1, 16184.

[20]   H. Liang, A. N. Gandi, D. H. Anjum, X. Wang, U. Schwingenschlögl, H. N. Alshareef, *Nano Lett.* **2016**, 16, 7718.

[21]   F. Dionigi, P. Strasser, *Adv. Energy Mater.* **2016**, 6, 1600621.

[22]   J. R. Swierk, S. Klaus, L. Trotochaud, A. T. Bell, T. D. Tilley, *J. Phys. Chem. C* **2015**, 119, 19022.

[23]   Y. Guo, Y. Tong, P. Chen, K. Xu, J. Zhao, Y. Lin, W. Chu, Z. Peng, C. Wu, Y. Xie, *Adv. Mater.* **2015**, 27, 5989.

[24]   P. W. Menezes, S. Yao, R. Beltrán-Suito, J. N. Hausmann, P. V. Menezes, M. Driess, *Angew. Chem., Int. Ed.* **2021**, 60, 4640.

1 [25] B. S. Yeo, A. T. Bell, *J. Phys. Chem. C* **2012**, 116, 8394.

2 [26] X. Su, Y. Wang, J. Zhou, S. Gu, J. Li, S. Zhang, *J. Am. Chem. Soc.* **2018**, 140, 11286.

3 [27] M. Gorlin, P. Chernev, J. Ferreira de Araujo, T. Reier, S. Dresp, B. Paul, R. Krahnert,

4   H. Dau, P. Strasser, *J. Am. Chem. Soc.* **2016**, 138, 5603.

5 [28] M. K. Bates, Q. Jia, H. Doan, W. Liang, S. Mukerjee, *ACS catal.* **2016**, 6, 155.

6 [29] N. Li, D. K. Bediako, R. G. Hadt, D. Hayes, T. J. Kempa, F. von Cube, D. C. Bell, L.

7   X. Chen, D. G. Nocera, *PNAS* **2017**, 114, 1486.

8 [30] D. Wang, J. Zhou, Y. Hu, J. Yang, N. Han, Y. Li, T.-K. Sham, *J. Phys. Chem. C* **2015**,

9   119, 19573.

10 [31] A. Govind Rajan, J. M. P. Martirez, E. A. Carter, *J. Am. Chem. Soc.* **2020**, 142, 3600.

11 [32] a) J. P. Perdew, K. Burke, M. Ernzerhof, *Phys. Rev. Lett.* **1996**, 77, 3865; b) W. Kohn,

12   L. J. Sham, *Phys. Rev.* **1965**, 140, A1133; c) G. Kresse, J. Furthmüller, *Comput.*

13   *Mater. Sci.* **1996**, 6, 15; d) G. Kresse, J. Furthmüller, *Phys. Rev. B* **1996**, 54, 11169.

14 [33] P. E. Blöchl, *Phys. Rev. B* **1994**, 50, 17953.

15 [34] S. Grimme, J. Antony, S. Ehrlich, H. Krieg, *J. Chem. Phys.* **2010**, 132, 154104.

16 [35] S. L. Dudarev, G. A. Botton, S. Y. Savrasov, C. J. Humphreys, A. P. Sutton, *Phys.*

17   *Rev. B* **1998**, 57, 1505.

18
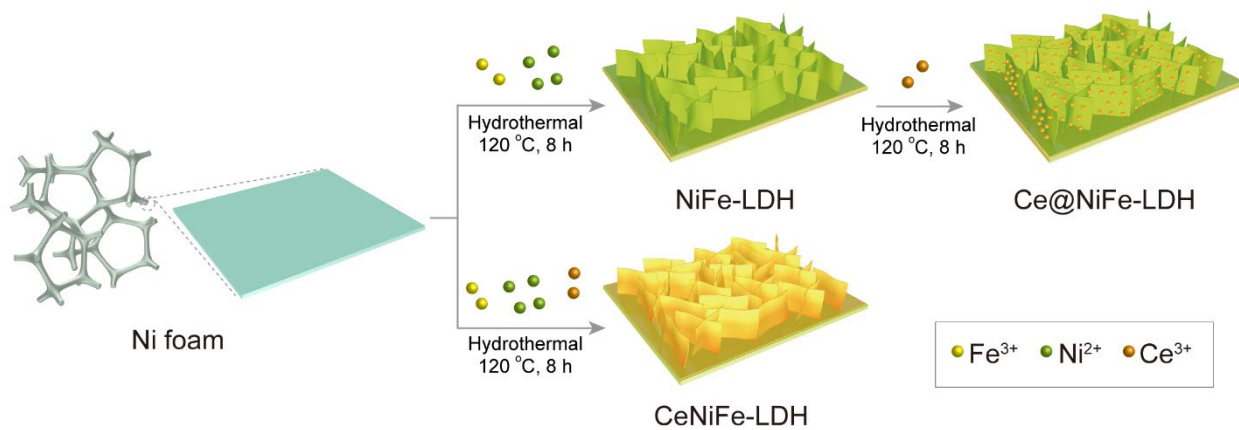
1

2 **Figure 1.** Schematic illustration of the synthetic procedures for NiFe-LDH, Ce@NiFe-LDH,

3 and CeNiFe-LDH nanosheet arrays.

4
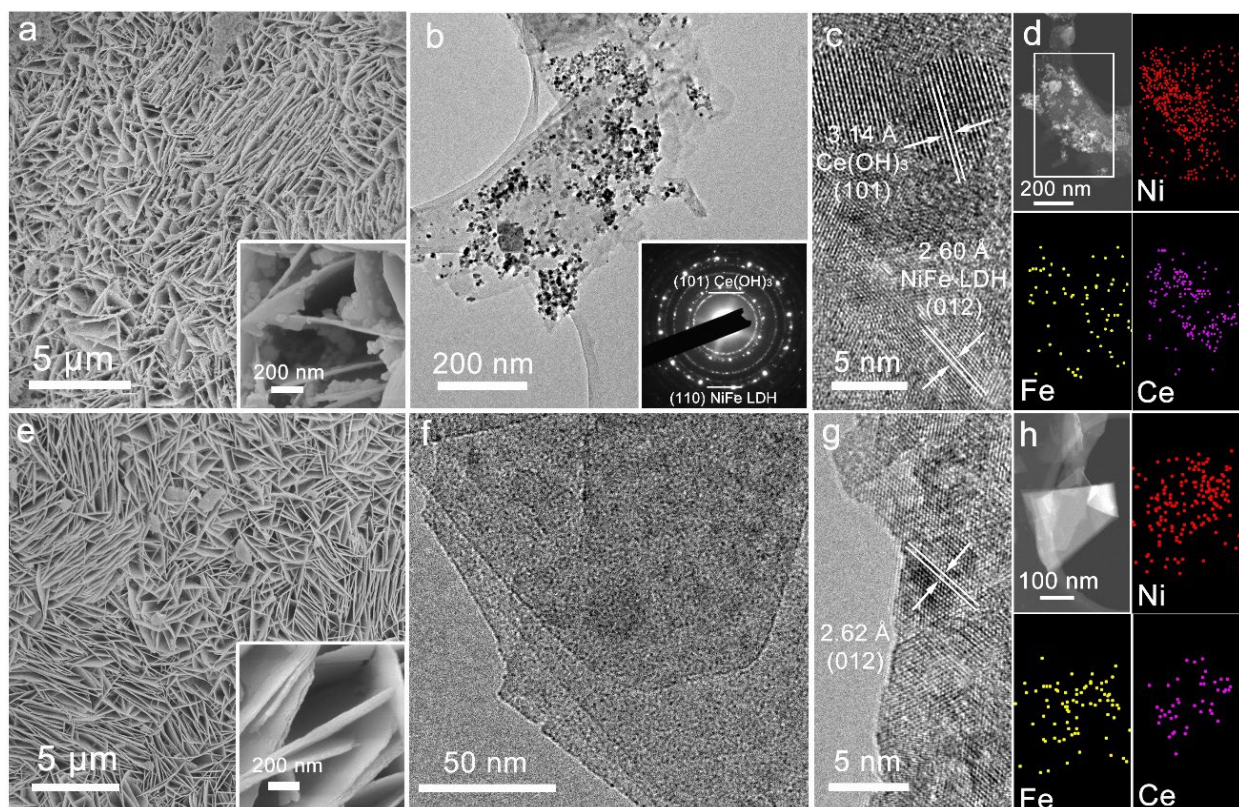
Figure 2. SEM images of (a) Ce@NiFe-LDH and (e) CeNiFe-LDH nanosheet arrays. Insets are the corresponding high-magnification SEM images. Low- and high-resolution TEM images of (b and c) Ce@NiFe-LDH and (f and g) CeNiFe-LDH nanosheets. Inset in (b) is the corresponding SAED pattern. HAADF-STEM images and the corresponding EDX elemental mappings of (d) Ce@NiFe-LDH and (h) CeNiFe-LDH.
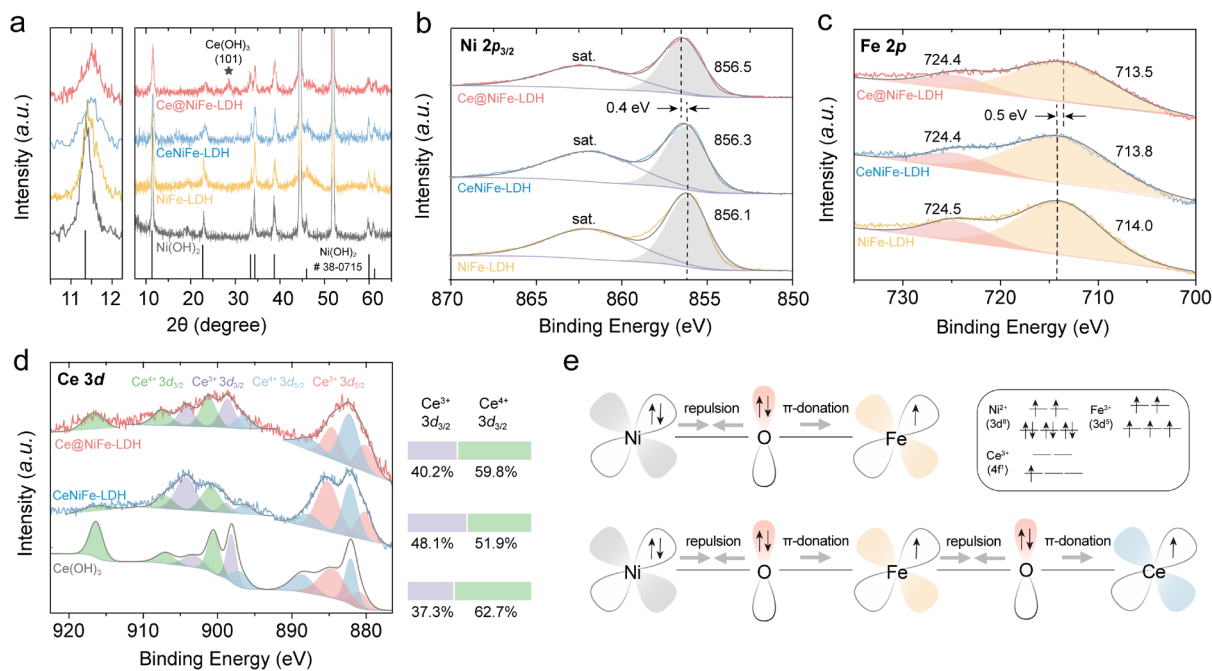
Figure 3. (a) XRD patterns and high-resolution XPS spectra of as-prepared Ce@NiFe-LDH and CeNiFe-LDH in (b) Ni $2p_{3/2}$, (c) Fe $2p$, and (d) Ce $3d$ regions. The data for Ni(OH)$_2$, NiFe-LDH, and Ce(OH)$_3$ are shown for comparison. Bars in (d) indicate the percentages of Ce^{3+} and Ce^{4+} in $3d_{3/2}$ region. (e) Schematics of the electronic interplay among Ni, Fe, Ce, and O in NiFe-LDH, CeNiFe-LDH, and Ce@NiFe-LDH.
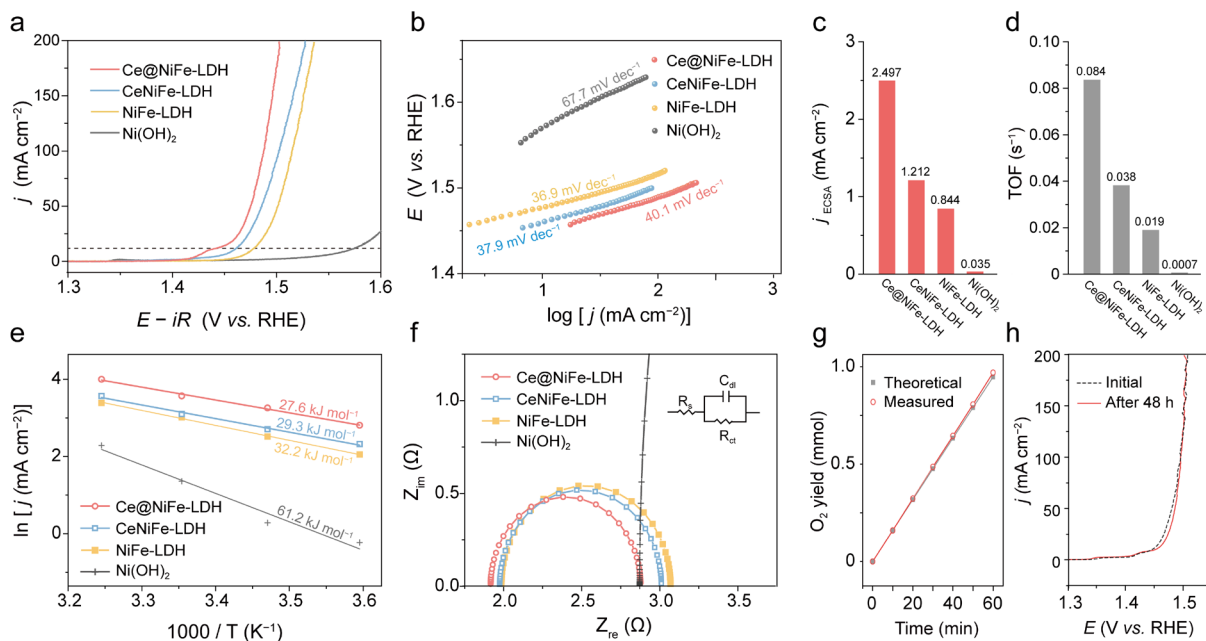
Figure 4. Electrochemical properties of Ce@NiFe-LDH, CeNiFe-LDH, NiFe-LDH, and Ni(OH)$_2$. (a) Linear polarization curves, (b) the corresponding Tafel plots, (c) current densities at 1.5 V (normalized by ECSA), (d) turnover frequencies (TOFs), (e) Arrhenius plots of kinetic currents at 0.3 V, and (f) Nyquist plots obtained at 1.5 V. Inset in (f) is the equivalent circuit. (g) Measured O$_2$ yields at 0.3 V and (h) polarization curves of Ce@NiFe-LDH before and after 48-h electrolysis. Theoretical curve is shown in (g) for Faradaic efficiency calculation.
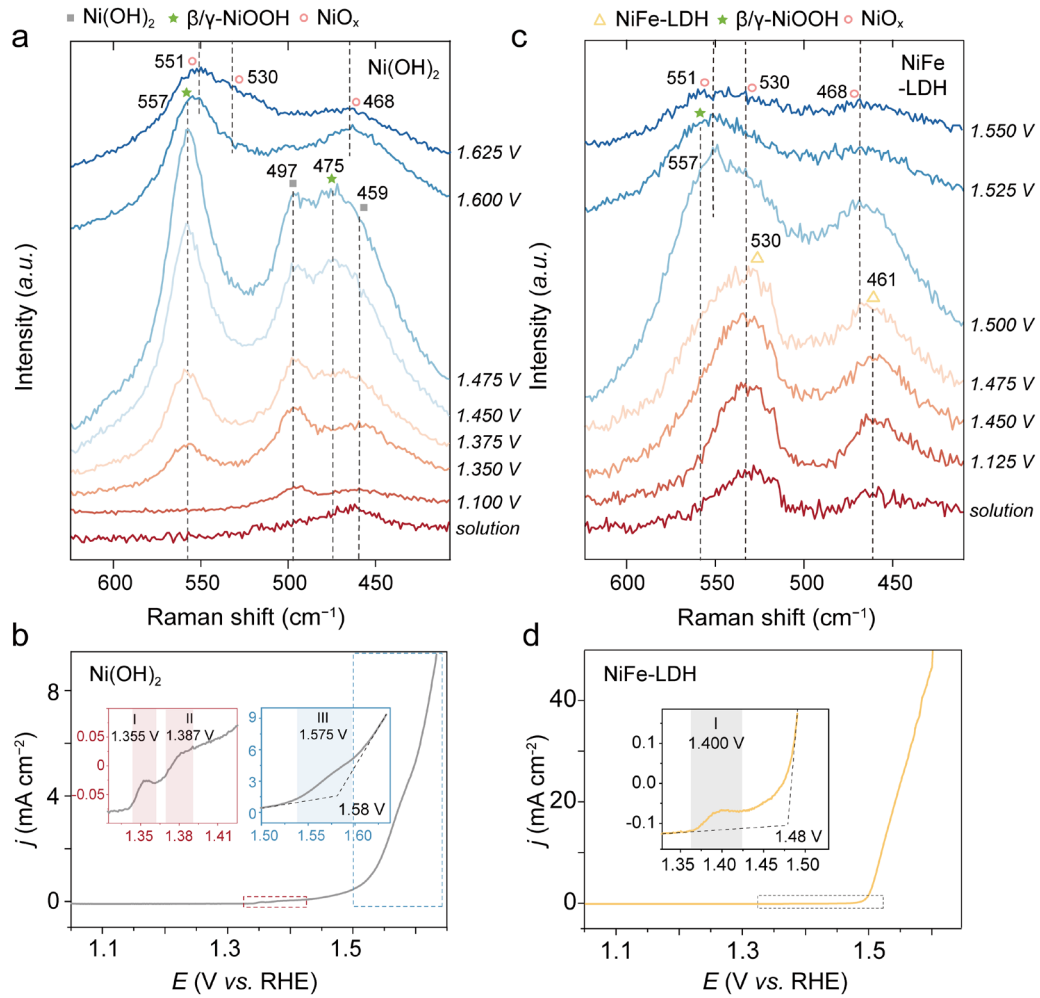
Figure 5. *Operando* Raman spectra of (a) Ni(OH)$_2$ and (b) NiFe-LDH under various applied potentials. The corresponding polarization curves of (c) Ni(OH)$_2$ and (d) NiFe-LDH. Scan rate is 0.3 mV s^{-1}. Insets show the LSV curves magnified at the redox peak and onset potentials.

30
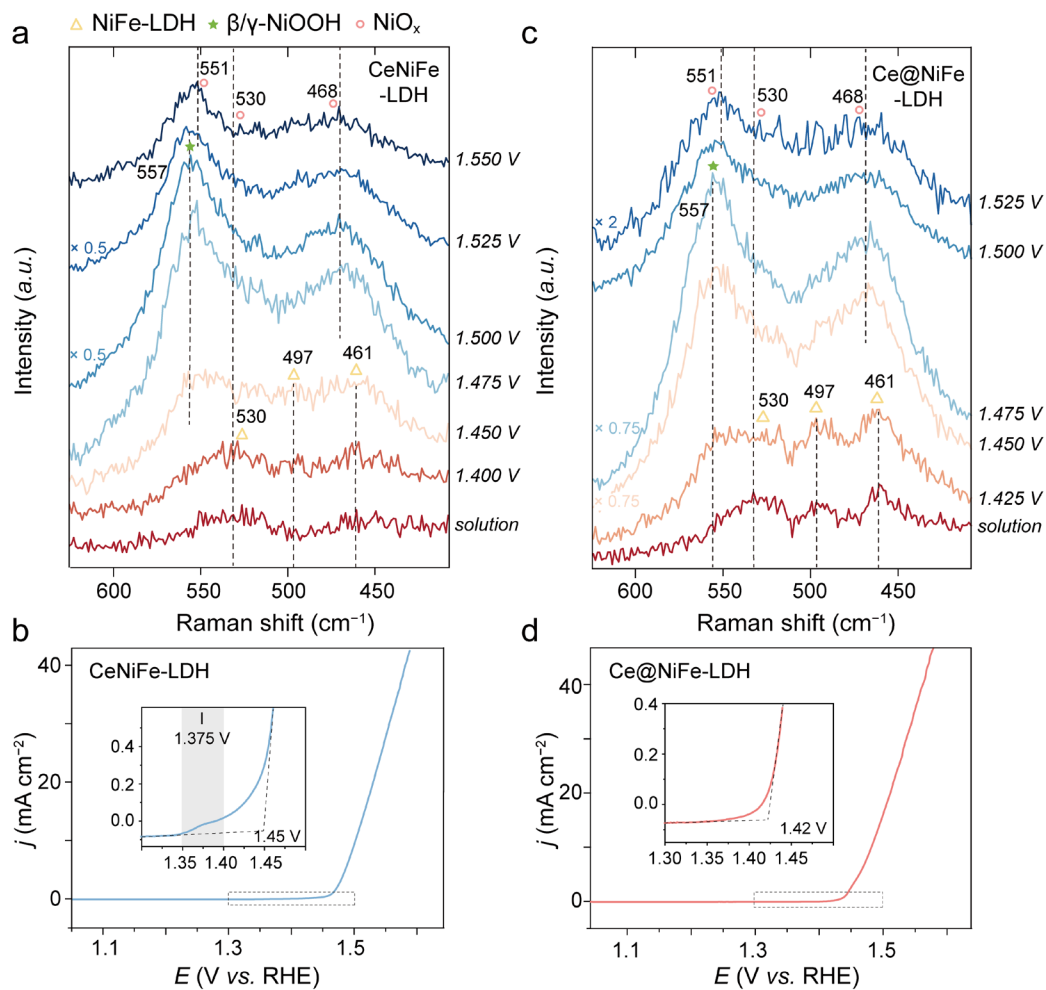
Figure 6. *Operando* Raman spectra of (a) CeNiFe-LDH and (b) Ce@NiFe-LDH under various applied potentials. The corresponding polarization curves of (c) CeNiFe-LDH and (d) Ce@NiFe-LDH. Scan rate is 0.3 mV s^{-1}. Insets show the LSV curves magnified at the redox peak and onset potentials.
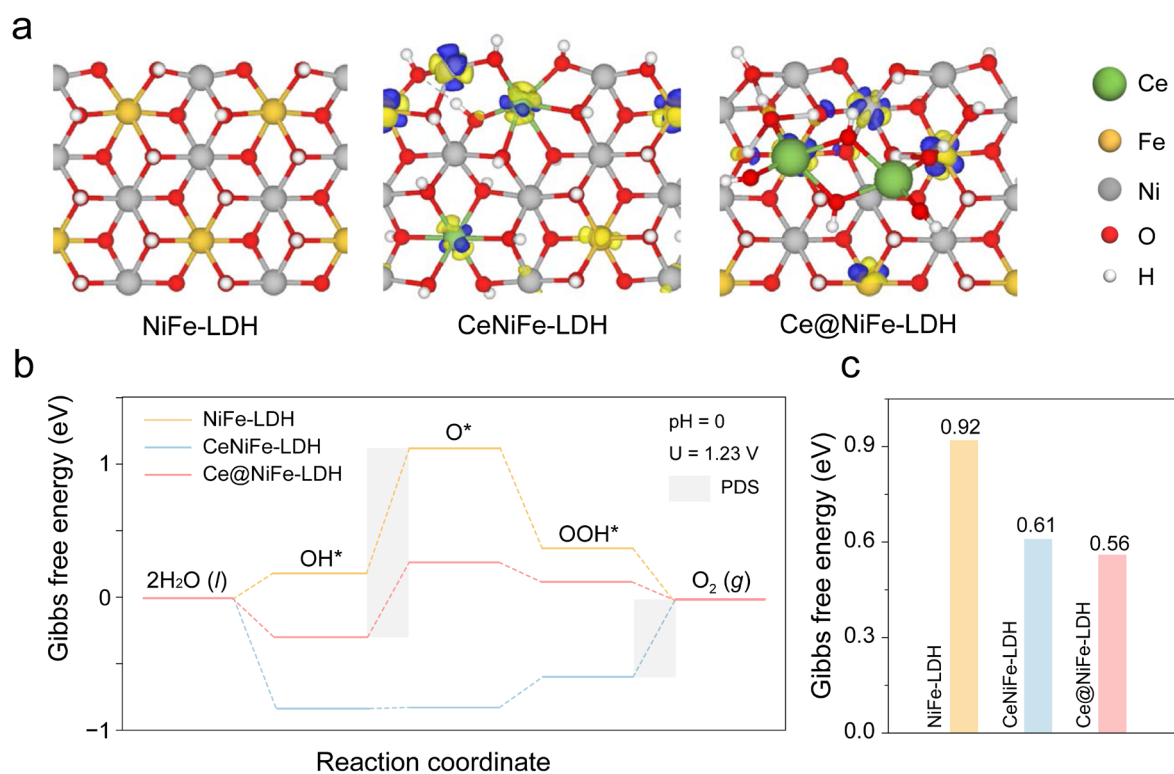
Figure 7. (a) NiFe-LDH (left), CeNiFe-LDH (middle) and Ce@NiFe-LDH (right) model systems for DFT calculations. We used Ni-terminated (110) surface due to its lowest surface energy. Charge density difference is shown, yellow and blue bubbles represent charge accumulation and depletion regions, respectively. (b) Gibbs free energy diagram of OER steps on models at U = 1.23 V (pH = 0, T = 298 K). (c) Gibbs free energy differences for rate-determining step (RDS) of models.
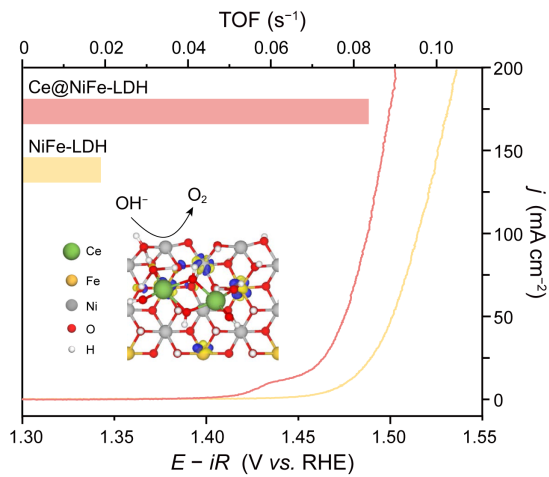
1 **Table of Contents Materials**

2 Two NiFe-LDHs doped with Ce (CeNiFe-LDH) and interfaced with $Ce(OH)_3$ (Ce@NiFe-

3 LDH) are studied to reveal the enhancement mechanism of water oxidation. In the Ce-modified

4 NiFe-LDHs, Ce and Fe atoms serve as the electron acceptors and facilitate the coupled

5 oxidation of $Ni^{3+/4+}$ in NiFe-LDH. Dissimilar charge redistribution in CeNiFe-LDH and

6 Ce@NiFe-LDH is revealed, which accounts superior catalytic activity for water oxidation.

7
8 Mengjie Liu, Kyung-Ah Min, Byungchan Han,* and Lawrence Yoon Suk Lee*
9
10 **Interfacing or Doping? Role of Ce in Highly Promoted Water Oxidation of NiFe-Layered**
11 **Double Hydroxide**
12

13